

PI = polyisoprene
PS = polystyrene
1, 2, 3, 4 = region

Literature Cited

- 1) Ballard, D. G. H., G. D. Wignall and J. Schelten: *Eur. Polym. J.*, **9**, 965 (1973).
- 2) Flory, P. J.: *J. Chem. Phys.*, **9**, 660 (1941); **10**, 51 (1942).
- 3) Flory, P. J.: "Principles of Polymer Chemistry," Cornell Univ. Press, Ithaca, New York (1953).
- 4) Funabashi, H., Y. Miyamoto, Y. Isono, T. Fujimoto, Y. Matsushita and M. Nagasawa: *Macromolecules*, **16**, 1 (1983).
- 5) Hashimoto, T., M. Fujimura and H. Kawai: *Macromolecules*, **13**, 1660 (1980).
- 6) Hashimoto, T., N. Nakamura, M. Shibayama, A. Izumi and H. Kawai: *Macromolecules Sci., Phys.*, **B17**, 389 (1980).
- 7) Huggins, M. L.: *J. Phys. Chem.*, **9**, 440 (1941).
- 8) Leibler, L., H. Orland and J. C. Wheeler: *J. Chem. Phys.*, **79**, 3550 (1983).
- 9) Noolandi, J. and K. M. Hong: *Macromolecules*, **16**, 1443 (1983).
- 10) Rounds, N. A.: Doctoral Dissertation, Univ. Akron (1971).
- 11) Whitmore, M. D. and J. Noolandi: *Macromolecules*, **18**, 657 (1985).

EFFECTS OF POST-IMPREGNATION DRYING CONDITIONS ON PHYSICAL PROPERTIES AND OVERALL REACTION RATE OF NICKEL/ALUMINA CATALYSTS

YOSHIMITSU UEMURA, YASUO HATATE AND ATSUSHI IKARI

Department of Chemical Engineering, Kagoshima University, Kagoshima 890

Key Words: Chemical Reaction, Nickel Alumina Catalyst, Impregnation, Drying, Pore Structure, Intracatalyst Activity Profile, Effectiveness Factor, Benzene Hydrogenation

The effects of post-impregnation drying conditions on the physical properties and overall rate of benzene hydrogenation were investigated with nickel/alumina catalysts, prepared by impregnating nickel ion-adsorptive and nickel ion-nonadsorptive aluminas and drying them under two conditions. Uniform nickel concentration profiles were obtained with the adsorptive support independent of the drying conditions, but the reduction degree of nickel by hydrogen and the nickel particle diameter were influenced by the drying conditions. With the nonadsorptive support, the drying conditions have a significant effect on the nickel profiles. In this case, the reduction degree and the particle diameter are dependent on the local all-nickel (reduced and unreduced nickel) content. The pore structure of the catalysts prepared from the nonadsorptive support was affected by the drying conditions. The experimental results of the overall reaction rate of benzene hydrogenation were found to be consistent with the change of the pore structure.

Introduction

Impregnation is one of the most important industrial methods for preparing supported catalysts. To obtain effective catalysts by impregnation, it is necessary to relate the physical properties and reactivity of the catalysts to the preparation conditions. Vincent *et al.*²³⁾ and Komiyama *et al.*¹⁵⁾ quantitatively investigated the transport phenomena of active components within the pores of the support. Bartholomew *et al.*¹⁾ reported the effects of calcination and reduction on the nickel morphology in nickel/alumina catalysts. Since a basic analytical study of the effectiveness factor of catalysts with

nonuniform activity profiles was accomplished by Kasaoka *et al.*,¹³⁾ some analytical investigations^{2,3,12)} of more complex cases have been reported. Recently, some unique information and techniques, e.g., pore size control of alumina by the pH swing method,¹⁸⁾ measurement¹⁴⁾ of the radial profiles of nickel particle diameter in nickel/alumina catalysts, and the deformation⁷⁾ of radial molybdenum profiles with molybdenum/alumina catalysts by high temperature calcination, were reported. However, few investigations⁸⁾ involving the preparation, physical properties, and reactivity of impregnated catalysts are found. Especially, there is little information on the effects of post-impregnation drying conditions on the physical properties and reactivity of the catalysts.

In a previous study,²²⁾ we investigated nickel-

Received April 30, 1986. Correspondence concerning this article should be addressed to Y. Uemura.

support interactions in nickel/alumina impregnated catalysts with all-nickel content ranging from 0.01 to 8.3 wt%. The term "all-nickel" means reduced and unreduced nickel in this paper. We showed that the intrinsic rate of benzene hydrogenation was proportional to the nickel surface area of nickel/alumina catalysts. From these results, it was confirmed that the activity profile of nickel/aluminas prepared by similar procedures could be estimated from only the nickel surface area distribution within the catalyst particle.

In the present study, the effects of the drying conditions and support characteristics on the physical properties (the all-nickel concentration profile, the nickel particle diameter, the reduction degree of nickel, and the pore size distribution) and overall reaction rate of benzene hydrogenation with impregnated nickel/alumina catalysts were investigated by a series of experiments involving preparation of the catalysts, measurements of the physical properties, and the reaction. Also, the activity profile functions of the catalysts were determined from the nickel surface area to predict the relationships between effectiveness factor and Thiele modulus.

1. Experimental

1.1 Preparation of catalysts

The physical properties of the supports used and the preparation conditions of nickel/alumina catalysts are presented in **Table 1**. Four kinds of nickel/alumina catalysts were prepared by using two kinds of spherical alumina supports (JRC-ALO-1 and JRC-ALO-3 supplied by Catalysis Society of Japan) and applying two drying conditions (fast and slow drying).

1) Impregnation The spherical aluminas, ALO-1 and ALO-3, were impregnated with nickel chloride aqueous solution till the adsorption equilibrium of nickel ion on the aluminas was reached. ALO-1 adsorbs no nickel ion, whereas ALO-3 does so, as shown in Table 1. The initial concentration of the impregnant and the support-impregnant ratio for both supports, shown in Table 1, were determined so as to obtain almost the same nickel content in all the catalysts.

2) Drying and reduction After impregnation, about half of the impregnated alumina was dried quickly by nitrogen gas fluidization. The rest was dried slowly under flowing nitrogen gas. Schematic diagrams of the drying apparatuses are shown in **Figs. 1 and 2**. The fluidized drying apparatus (Fig. 1) consists of gas flow rate controls (1, 2, 3), drier (5), and humidity detector (6, 7). The drier (5) made from Pyrex glass is tubular with an internal diameter of 26 mm, and its temperature is maintained at a desired value by an electric furnace (4) and a temperature controller (8). After attaining desired gas flow rate

and temperature, the impregnated support was charged from the top of the drier. The humidity of effluent gas was monitored continuously by the detector during drying. As no humidity was detected, drying was terminated. The flow drying apparatus consists of the control system of gas flow rate for drying (1, 3, 4), that for dilution (2, 3, 4), drier (8), and humidity detector (11, 12). The drier (8) is a Pyrex glass tube with an internal diameter of 26 mm, in which the sample holder (7) made of stainless net is suspended from the sleeve of the thermocouple. To prevent one-side drying, the impregnated support in the holder is made to rotate slowly by a vibrator (6) during drying. Drying was carried out by a similar procedure to that of fluidized drying.

About 0.02 kg of the dried sample was placed in a flow-through Pyrex tube with an internal diameter of 15.5 mm to permit reduction in flowing pure hydrogen gas. Before each reduction run, the sample was pretreated under flowing pure nitrogen ($100 \text{ cm}^3 \cdot \text{min}^{-1}$) at 378 K for 1 h to control the initial state of the reduction run. The sample was raised from 378 to 723 K at a rate of $6 \text{ deg} \cdot \text{min}^{-1}$ under flowing pure hydrogen ($200 \text{ cm}^3 \cdot \text{min}^{-1}$) and then reduced under the same atmosphere at 723 K for 17 h. After reduction, a part of the spherical catalysts with an average diameter of $3100 \mu\text{m}$ was crushed and sieved. A series of catalysts, ranging from 119 to $3100 \mu\text{m}$ in average diameter, was obtained for each original catalyst.

1.2 Physical properties of catalysts

The all-nickel content on each catalyst was determined by a chelate titration. The reduced-nickel content was determined by TGA. The all-nickel concentration profiles were measured by EPMA. TEM was applied to determine the nickel particle size distribution and the average in the catalysts. The measurement procedures were described in the previous paper.²²⁾ The pore volumes of the supports and the catalysts were measured by a mercury porosimeter Model 2030 (Carlo Erba Strumentazione) with pressure ranging from 0.1 to 200 MPa. A 200- to 300-mg bead-form sample was used.

1.3 Hydrogenation of benzene

The reaction was carried out with the nickel/alumina catalysts in an atmospheric flow system with a fixed-bed reactor. The reactor was made from Pyrex tube with an internal diameter of 10 mm. A series of catalysts ranging from 119 to $3100 \mu\text{m}$ in average diameter was used. The reaction kinetics was determined by using the catalysts with an average diameter of $119 \mu\text{m}$.

A 50- to 200-mg sample of the catalyst was packed in the reactor. The bed volume of the catalyst ranged from 0.1 to 0.4 cm^3 . The catalyst was pretreated under flowing pure hydrogen gas at 673 K for 1 h, and then

Table 1. Preparation of catalysts

	A1F	A1S	A3F	A3S
Support		JRC-ALO-1		JRC-ALO-3
form		white bead		white bead
composition ⁵⁾		$\eta + \gamma$ -alumina		γ -alumina
BET surface area [$\text{m}^2 \cdot \text{kg}^{-1}$] ⁴⁾		1.69×10^5		1.21×10^5
model pore diameter [nm] ⁵⁾		9.0		10.0
specific pore volume [$\text{m}^3 \cdot \text{kg}^{-1}$] ⁵⁾		6.70×10^{-4}		5.28×10^{-4}
average diameter [mm]		3.1		3.1
nickel ads. n_0 [$\text{mol} \cdot \text{kg}^{-1}$]		0		0.194
K [$\text{l} \cdot \text{mol}^{-1}$]		—		236
Impregnation		NiCl_2 aq. solution (308 K)		
concentration [$\text{mol} \cdot \text{l}^{-1}$]		0.237		0.151
support-impregnant ratio [$\text{kg} \cdot \text{l}^{-1}$]		0.59		0.62
Drying	fluidization by nitrogen	under flowing nitrogen	fluidization by nitrogen	under flowing nitrogen
temp. during constant rate [K]	340 (0–2 min)	333	345 (0–2 min)	333
during falling rate [K]	390 (2–10)	333	365 (2–10)	333
during dry-up [K]	455 (10–24)	333	405 (10–20)	333
gas velocity [$\text{m} \cdot \text{s}^{-1}$]	2.4	4.6×10^{-4}	2.8	4.6×10^{-4}
W/F [$\text{kg} \cdot \text{s} \cdot \text{m}^{-3}$]	19	3.0×10^3	18	3.3×10^3
time [min]	24	600	20	600
Reduction	under flowing hydrogen gas (723 K, 17 h)			

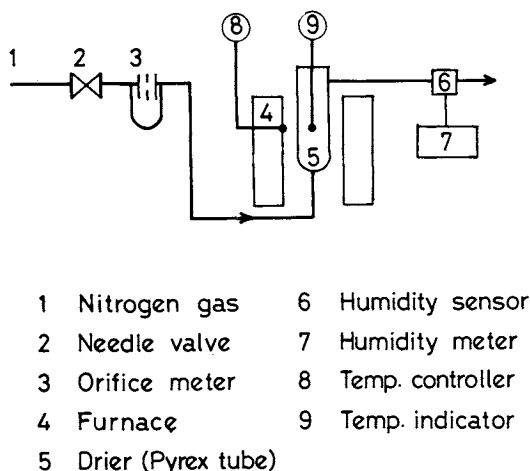


Fig. 1. Schematic diagram of fluidized drying apparatus.

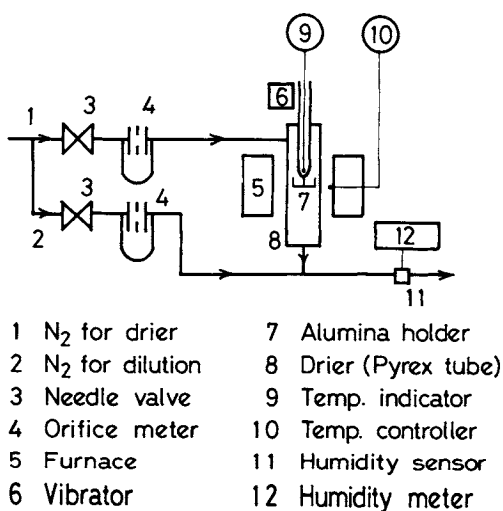


Fig. 2. Schematic diagram of flow drying apparatus.

the catalyst bed was cooled down to reaction temperature ranging from 473 to 503 K. Next, the reactant gases (benzene and hydrogen) and nitrogen were allowed to flow through the catalyst bed. The partial pressure of benzene ranged from 1.1 to 5.5 kPa and that of hydrogen from 50.6 to 81.0 kPa. The space velocity ranged from 20 to 80 s⁻¹. Reactor effluent gas was injected into a gas chromatograph via a microvolume sampling valve. Cyclohexene and cyclohexane were detected as reaction products. The reaction rate of the first step, benzene to cyclohexene, was considered in studying the reactivity of the catalysts.

2. Results and Discussion

2.1 Effect of drying conditions on physical properties

1) All-nickel concentration profile Only A1F (3100 μm), prepared by using nonadsorptive alumina and applying fast drying, showed an uneven profile (shell type). Uniform profiles were observed for the other spherical catalysts. Such an uneven profile, observed in the case of fast drying, was previously reported by some workers.^{8,15)} Redistribution of the impregnant solution within the pore causes it.¹⁵⁾

2) All-nickel content and reduction degree of nickel All-nickel content and reduction degree of nickel in the catalysts are presented in Table 2. The all-nickel contents from a chelate titration show similar values among all the catalysts. On the other hand, the reduction degree of nickel ranges from 0.4 to 0.6. Many workers reported that the reduction degree of nickel in nickel/alumina catalysts was smaller than unity.^{1,19)} The results suggest that the reduction degree of nickel is influenced by the dry-

Table 2. Physical properties of catalysts

	A1F	A1S	A3F	A3S
All-nickel content [wt%]	1.10	1.07	1.09	1.05
Reduced-nickel content [wt%]	0.617	0.434	0.492	0.551
Reduction degree of nickel [—]	0.561	0.406	0.451	0.525
Nickel particle diameter [nm]* ¹	17.2* ² 18.9* ³ 32.9* ⁴	26.7	17.8	15.2
Nickel surface area [m ² ·kg ⁻¹]	175	110	187	246
Nickel concentration profile	shell	uniform	uniform	uniform

*¹ Volume-area mean.
*² $r/R=0-0.5$.
*³ $r/R=0.5-0.77$.
*⁴ $r/R=0.93-1$.

ing rate and the support characteristics. In the previous study²²⁾ with nickel/ALO-1 catalysts, we showed that the reduction degree of nickel and the average nickel particle diameter were represented as a function of local all-nickel content. The expressions are as follows.

$$f_R(w'_i) = 0.50 w'_i(x)^{0.371} \quad (0.71 \leq w'_i \leq 2.54) \quad (1)$$

$$= 0.65 w'_i(x)^{0.109} \quad (2.54 < w'_i \leq 8.25) \quad (2)$$

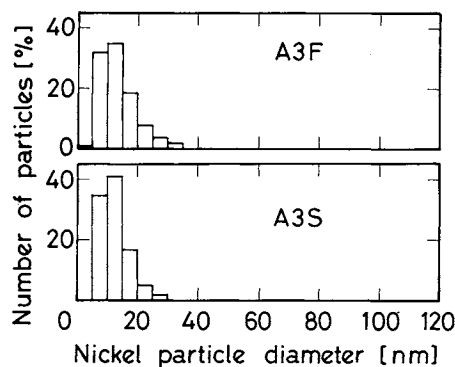
$$\bar{D}_{32}(w'_i) = 2.0 \times 10^{-8} w'_i(x)^{0.624} \quad (0.65 \leq w'_i \leq 8.25) \quad (3)$$

The equations are applicable to A1F and A1S.

The reduction degree of nickel of A3F is smaller than that of A3S. Some previous studies^{1,19)} with nickel/alumina catalysts indicated that nickel would interact with alumina strongly. The exposure of A3F precursor to higher temperatures during drying would cause a stronger nickel-alumina interaction and lower reduction degree.

3) **Nickel particle diameter** The nickel particle size distributions of A3F and A3S from TEM are shown in **Fig. 3**. Fast drying (A3F) causes broad nickel particle size distribution and large average value compared with slow drying (A3S). For A1F and A1S, the distributions were shown in the previous paper (Fig. 7(b)).²²⁾ The volume-area mean diameters are presented in Table 2.

4) **Pore volume** The pore volumes of the catalysts and the supports from mercury porosimetry are presented in **Table 3**. The results indicate that A1F and A1S have different pore structures from that of ALO-1. The pore volume of A1F and A1S with pore diameter ranging from 7 to 110 nm is larger than that of ALO-1, and the volume from 110 to 1100 nm is smaller than that of ALO-1. The extent of the difference increases with the post-impregnation drying rate.

**Fig. 3.** Nickel particle size distributions of A3F and A3S.**Table 3.** Pore volume from mercury porosimetry

$V_p \times 10^4$ [m ³ ·kg ⁻¹]	ALO-1	A1S	A1F	ALO-3	A3S	A3F
7–110 nm*	6.38	6.58	7.01	3.92	3.88	4.09
110–1100 nm*	0.90	0.74	0.47	0.77	0.80	0.75

* Range of pore diameter.

On the other hand, the pore structure of A3F and A3S are the same as that of ALO-3.

The surface of alumina contacted with water is hydrated. Dehydration of hydrated alumina, which is significant above 400 K,²⁰⁾ may cause decrease of macropore (intergranular pore) volume by intergranular sintering^{9,11)} and development of micropore by intragranular decomposition.⁶⁾ Such intergranular and intragranular dehydration result in a change of pore structure of A1F and A1S during post-impregnation drying. The larger extent of structural change in A1F compared with A1S is interpreted as a result of higher temperature during drying of A1F than that of A1S, as shown in Table 1. No structural change in the nickel/ALO-3 (A3F and A3S) may be attributed to the difference in raw material of ALO-3 and ALO-1.¹⁶⁾

2.2 Performance of catalysts with nonuniform activity

As described in 2.1, an uneven all-nickel concentration profile was obtained in the present study. For analysis of this case, the activity profile should be considered instead of the all-nickel concentration profile. In this section, the aspects of spherical catalyst performance with nonuniform activity profiles are discussed quantitatively.

1) **Effectiveness factor** From mass and energy balances in a spherical catalyst with a nonuniform activity profile, in which n th order reaction occurs, the following dimensionless equations are obtained.

$$\theta = 1 + (1 - c)\beta \quad (4)$$

$$\frac{1}{x^2} \frac{d}{dx} \left(x^2 \frac{dc}{dx} \right) = \phi^2 a(x) \exp \left[\frac{\varepsilon \beta (1 - c)}{1 + \beta (1 - c)} \right] c^n \quad (5)$$

The boundary conditions are:

$$dc/dx=0 \quad \text{at} \quad x=0 \quad (6)$$

$$c=1 \quad \text{at} \quad x=1 \quad (7)$$

The parameters used above are defined as follows.

$$c=C/C_0; \quad \theta=T/T_0; \quad x=r/R;$$

$$k_{v0}=A_v \exp(-E/R_g T_0); \quad \phi^2=R^2 k_{v0} C_0^{n-1}/D_e;$$

$$\varepsilon=E/R_g T_0; \quad \beta=(-\Delta H)C_0 D_e/T_0 k_e$$

By solving the above equations, the reactant concentration and temperature profile within a spherical catalyst are obtained. The effectiveness factor can be calculated from the following equation.

$$\eta=3 \int_0^1 \exp\left[\frac{\varepsilon\beta(1-c)}{1+\beta(1-c)}\right] c^n a(x) x^2 dx \quad (8)$$

2) Activity profile function The activity profile function at radial distance x is proportional to the number of active sites per unit volume of a catalyst at x . For catalytic reactions with structure insensitivity, the number is proportional to the metal surface. Then the activity profile function is represented as follows.

$$\begin{aligned} a(x) &= k_a S(x) \\ &= k_a \frac{6}{D_{32}(w_t)} \frac{w_r(x)}{\rho_m} \end{aligned} \quad (9)$$

On the assumption that the apparent density of a spherical catalyst is constant regardless of radial distance, the following expression is derived from Eq. (9).

$$a(x) = k_a \frac{6}{D_{32}(w_t)} \frac{w'_r(x) f_R(w_t)}{100 \rho_m \rho_c} \quad (10)$$

The constant, k_a , is determined by the following relationship.

$$\int_0^1 a(x) x^2 dx = \frac{1}{3} \quad (11)$$

2.3 Kinetics of benzene hydrogenation

Figures 4, 5, 6, and 7 illustrate the intrinsic reaction rate of benzene hydrogenation using A1F (119 μm) and A3F (119 μm). Figure 8 shows Arrhenius plots for the reaction rate constants. From those results, the following rate equations are obtained.

A1F

$$r_m = 1.21 \times 10^{-13} \exp\left(\frac{41500}{R_g T}\right) p_B^{0.5} p_H^{2.5} \quad (12)$$

A3F

$$r_m = 2.23 \times 10^{-14} \exp\left(\frac{57100}{R_g T}\right) p_B^{0.5} p_H^{2.0} \quad (13)$$

In the present results, the intrinsic reaction rate

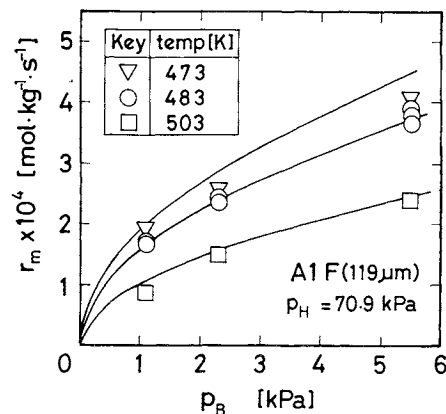


Fig. 4. Reaction rate of benzene hydrogenation as a function of benzene partial pressure for A1F (119 μm).

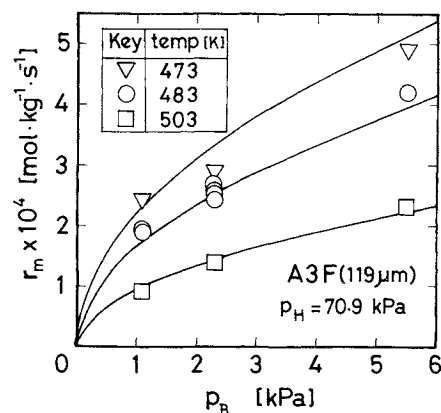


Fig. 5. Reaction rate of benzene hydrogenation as a function of benzene partial pressure for A3F (119 μm).

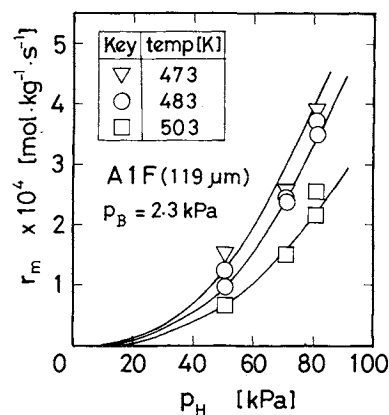


Fig. 6. Reaction rate of benzene hydrogenation as a function of hydrogen partial pressure for A1F (119 μm).

decreases with temperature. Such a tendency is common¹⁷⁾ in benzene hydrogenation, because the adsorbed amount of reactant on catalysts decreases with temperature.

2.4 Effectiveness factor of catalysts

To study the overall reaction rates of benzene hydrogenation, which were measured under conditions free from external mass transfer control, the

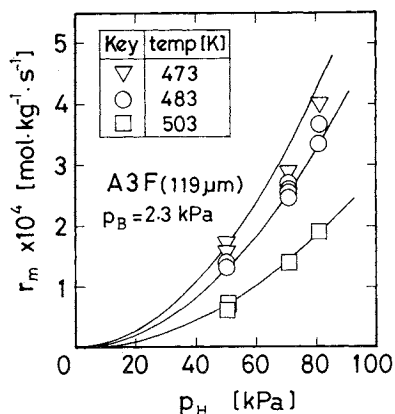


Fig. 7. Reaction rate of benzene hydrogenation as a function of hydrogen partial pressure for A3F (119 μm).

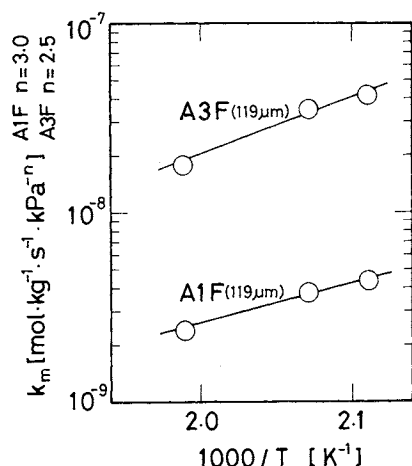


Fig. 8. Arrhenius plots for rate constant of benzene hydrogenation.

relationships between effectiveness factor and Thiele modulus are calculated by using the parameters in Table 4 and the activity profile in Fig. 9. The calculated effectiveness factor as a function of Thiele modulus is illustrated in Fig. 10. Calculated dimensionless temperatures, θ , were unity to the extent of five significant digits in the whole range of the present study. The result indicates that there is no significant nonuniformity of temperature within the catalyst particles in the present study. Figure 10 indicates that the catalysts with the "shell" profile have a larger effectiveness factor than that of catalysts with the "uniform" profile at the same value of Thiele modulus.

The experimental results for effectiveness factors, determined by dividing the overall reaction rate by that of catalyst with an average diameter of 119 μm , are plotted against the average particle radius in Figs. 11 and 12. These results indicate that there is no internal diffusion control for A3F and A3S, while the effectiveness factors of A1F (3100 μm) and A1S (3100 μm) show considerable decrease. The curves in Fig. 11 were drawn by adjusting ϕ/R to obtain the

Table 4. Model parameters for calculation of effectiveness factor

	A1F (bead)	A1F (crushed) A1S (bead, crushed)	A3F, A3S (bead, crushed)
Parameter type	I	II	III
$a(x)$ [—]	shell* ²	uniform* ²	uniform* ²
n [—]	0.5	0.5	0.5
ε [—]	−10.33	−10.33	−14.22
β [—]	2.4×10^{-4}	2.4×10^{-4}	2.7×10^{-4}
E [J·mol ^{−1}]	-4.15×10^4	-4.15×10^4	-5.71×10^4
T_0 [K]	483	483	483
$-\Delta H$ [J·mol ^{−1}]	2.15×10^5	2.15×10^5	2.15×10^5
C_0 [mol·m ^{−3}]	0.572	0.572	0.572
k_e [J·m ^{−1} ·s ^{−1} ·K ^{−1}] ²¹	0.22	0.22	0.22
D_e [m ² ·s ^{−1}] ^{*1}	2.1×10^{-7}	2.1×10^{-7}	2.3×10^{-7}

*¹ Calculated from Knudsen and molecular diffusion coefficient on the assumption that (porosity/tortuosity)=0.1. (Knudsen type is predominant in all cases.)

*² Illustrated in Fig. 9.

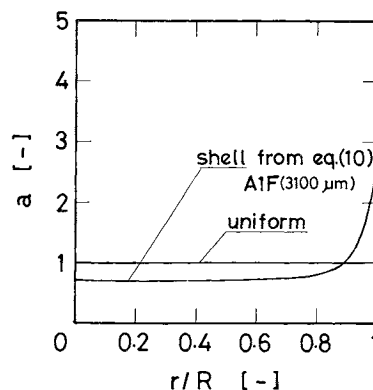


Fig. 9. Activity profile functions.

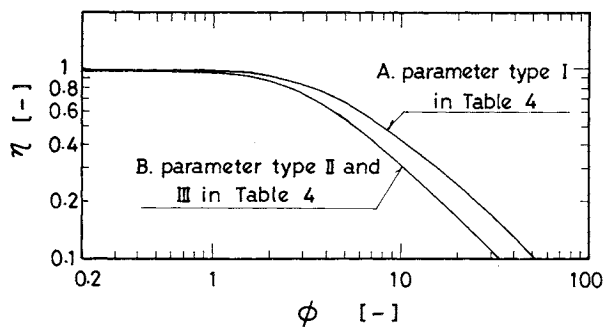


Fig. 10. Effectiveness factor calculated from model parameters shown in Table 4 and Fig. 9.

best fit between the calculated patterns in Fig. 10 and the experimental results. From those ϕ/R values, the effective diffusion coefficients were estimated as $2.9 \times 10^{-9} \text{ m}^2 \cdot \text{s}^{-1}$ for A1F and $4.5 \times 10^{-8} \text{ m}^2 \cdot \text{s}^{-1}$ for A1S. The difference of macropore volume between A1F and A1S as shown in Table 3 is presumably responsible for the smaller effective diffusion coefficient of A1F. On the assumption that the effective-

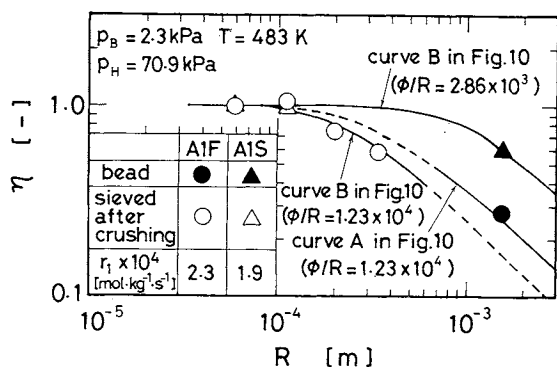


Fig. 11. Effectiveness factor as a function of catalyst particle radius for A1F and A1S.

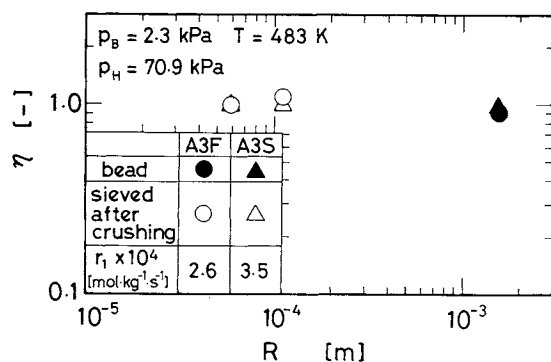


Fig. 12. Effectiveness factor as a function of catalyst particle radius for A3F and A3S.

ness factors for the nickel/ALO-3 catalysts with an average diameter of $3100 \mu\text{m}$ are larger than 0.90 in consideration of experimental error, the effective diffusion coefficients are obtained as above $4.2 \times 10^{-7} \text{m}^2 \cdot \text{s}^{-1}$ for A3F and above $5.5 \times 10^{-7} \text{m}^2 \cdot \text{s}^{-1}$ for A3S from the result in Fig. 12. The effective diffusion coefficients for A3F and A3S are larger than those for A1F and A1S. The result is consistent with the study of Inui *et al.*,¹⁰⁾ in which ALO-3 has a larger effective diffusion coefficient than ALO-1.

Conclusion

Four kinds of nickel/alumina catalysts were prepared by using nickel ion-nonadsorptive (ALO-1) and nickel ion-adsorptive (ALO-3) aluminas, and applying two drying conditions. Measurements and analyses of the physical properties and the reaction rate of benzene hydrogenation led to the following conclusions.

1) Drying conditions show no significant effect on the all-nickel concentration profile in nickel/ALO-3, while fast drying causes a shell-type concentration profile in nickel/ALO-1.

2) Fast drying would make the reduction degree of nickel/ALO-3 lower due to the acceleration of the nickel-support interaction at higher temperatures

than that of slow drying. The reduction degree of nickel/ALO-1 would depend on the local all-nickel content, the profile of which is influenced by the drying conditions.

3) The variance of the nickel particle size distribution and the average of the nickel/ALO-3 increase with drying rate. For nickel/ALO-1, both the nickel particle size distribution and its average are dependent on the local all-nickel content.

4) The pore structure of nickel/ALO-1 is affected by the drying condition, while such an influence is not observed for nickel/ALO-3.

5) The relationships between effectiveness factor and Thiele modulus calculated in consideration of activity profile function were found to be consistent with the experimental results. This suggests that the drying condition affects the effective diffusion coefficient of nickel/ALO-1.

Acknowledgment

The authors are very grateful to Professors F. Nakashio and S. Morooka of Kyushu University for their advice and support.

We also wish to thank the Technical Research Laboratory of Kagoshima Prefecture for permitting us to use its mercury porosimeter.

Nomenclature

A_v	= frequency factor per unit volume of catalyst	$[\text{mol}^{1-n} \cdot \text{m}^{3(n-1)} \cdot \text{s}^{-1}]$
$a(x)$	= activity profile function	[—]
C	= reactant concentration in catalyst particle	$[\text{mol} \cdot \text{m}^{-3}]$
C_0	= reactant concentration at surface of catalyst particle	$[\text{mol} \cdot \text{m}^{-3}]$
c	= dimensionless concentration of reactant	[—]
D_e	= effective diffusion coefficient of reactant	$[\text{m}^2 \cdot \text{s}^{-1}]$
D_p	= pore diameter	[nm]
$\bar{D}_{32}(w'_i)$	= volume-area mean diameter of metal particle as a function of w'_i	[m]
E	= activation energy	$[\text{J} \cdot \text{mol}^{-1}]$
F	= nitrogen gas flow rate in drier	$[\text{m}^3 \cdot \text{s}^{-1}]$
$f_R(w'_i)$	= reduction degree as a function of w'_i	[—]
$-\Delta H$	= heat of reaction	$[\text{J} \cdot \text{mol}^{-1}]$
K	= adsorption equilibrium constant of Langmuir isotherm	$[\text{l} \cdot \text{mol}^{-1}]$
k_m	= reaction rate constant per unit mass of catalyst	$[\text{mol} \cdot \text{kg}^{-1} \cdot \text{s}^{-1} \cdot \text{kPa}^{-\{ \text{total reaction order} \}}]$
k_{v0}	= reaction rate constant per unit volume of catalyst at T_0	$[\text{mol}^{1-n} \cdot \text{m}^{3(n-1)} \cdot \text{s}^{-1}]$
k_a	= constant defined in Eq. (11)	[m]
k_e	= thermal conductivity of catalyst particle	$[\text{J} \cdot \text{m}^{-1} \cdot \text{s}^{-1} \cdot \text{K}^{-1}]$
n	= order of reaction	[—]
n_0	= amount of saturation adsorption of Langmuir isotherm	$[\text{mol} \cdot \text{kg}^{-1}]$
P_B	= partial pressure of benzene	[kPa]
P_H	= partial pressure of hydrogen	[kPa]
R	= catalyst particle radius	[m]
R_g	= gas constant	$[\text{J} \cdot \text{mol}^{-1} \cdot \text{K}^{-1}]$
r	= radial distance from the center of catalyst particle	[m]

r_m	= intrinsic reaction rate per unit mass of catalyst	$[\text{mol} \cdot \text{kg}^{-1} \cdot \text{s}^{-1}]$
r_{m0}	= overall reaction rate per unit mass of catalyst	$[\text{mol} \cdot \text{kg}^{-1} \cdot \text{s}^{-1}]$
$S(x)$	= metal surface area per unit volume of catalyst at distance x	$[\text{m}^{-1}]$
T	= temperature	$[\text{K}]$
T_0	= temperature at surface of catalyst particle	$[\text{K}]$
V_p	= specific pore volume	$[\text{m}^3 \cdot \text{kg}^{-1}]$
W	= mass of impregnated support	$[\text{kg}]$
$w_r(x)$	= mass of reduced metal per unit volume of catalyst at distance x	$[\text{kg} \cdot \text{m}^{-3}]$
\bar{w}'_r	= average weight percent of reduced metal	$[\text{wt}\%]$
$w'_r(x)$	= weight percent of total metal at distance x	$[\text{wt}\%]$
x	= dimensionless radial distance	$[-]$
β	= dimensionless parameter defined as $(-\Delta H)C_0D_e/(T_0k_e)$	$[-]$
ε	= dimensionless parameter defined as $E/(R_gT_0)$	$[-]$
η	= effectiveness factor	$[-]$
θ	= dimensionless temperature	$[-]$
ρ_c	= apparent density of catalyst particle	$[\text{kg} \cdot \text{m}^{-3}]$
ρ_m	= density of metal	$[\text{kg} \cdot \text{m}^{-3}]$
ϕ	= Thiele modulus	$[-]$

Literature Cited

- Bartholomew, C. H. and R. J. Farrauto: *J. Catal.*, **45**, 41 (1976).
- Corbett, Jr. W. E. and D. Luss: *Chem. Eng. Sci.*, **29**, 1473 (1974).
- Dadyburjor, D. B.: *AIChE J.*, **28**, 720 (1982).
- Data-JRC-0001, Hattori, T.: *Shokubai (Catalyst)*, **22**, 115 (1980).
- Data-JRC-0002, Mukaida, K.: *Shokubai (Catalyst)*, **22**, 116 (1980).
- de Boer, J. H., A. van den Heuvel and B. G. Linsen: *J. Catal.*, **3**, 268 (1964).
- Duncombe, P. R. and S. W. Weller: *AIChE J.*, **31**, 410 (1985).
- Galiasso, R., O. L. de Ochoa and P. Andreu: *Appl. Catal.*, **5**, 309 (1983).
- Inoguchi, M., K. Tate, Y. Kaneko, Y. Satomi, K. Inaba, T. Mizutori, H. Kagaya, R. Nishiyama, S. Otani and T. Nagai: *Bull. Japan Petrol. Inst.*, **13**, 147 (1971).
- Inui, T., T. Miyake and Y. Takegami: *J. Japan Petrol. Inst.*, **25**, 242 (1982).
- Johnson, M. F. L. and J. Mooi: *J. Catal.*, **10**, 342 (1968).
- Juang, H.-D. and H.-S. Weng: *Ind. Eng. Chem.*, **22**, 224 (1983).
- Kasaoka, S. and Y. Sakata: *J. Chem. Eng. Japan*, **1**, 138 (1968).
- Komiyama, M. and R. P. Merrill: *J. Chem. Eng. Japan*, **18**, 381 (1985).
- Komiyama, M., R. P. Merrill and H. F. Harnsberger: *J. Catal.*, **63**, 35 (1980).
- Murakami, Y.: Preprints for the Third International Symposium on Scientific Bases for the Preparation of Catalysts, N2 (1982).
- Nagata, S., K. Hashimoto, I. Taniyama, H. Nishida and S. Iwane: *Kagaku Kōgaku*, **27**, 558 (1963).
- Ono, T., Y. Ohguchi and O. Togari: Preprints for the Third International Symposium on Scientific Bases for the Preparation of Heterogeneous Catalysts, G3 (1982).
- Peri, J. B.: *J. Catal.*, **86**, 84 (1984).
- Russell, A. S. and C. N. Cochran: *Ind. Eng. Chem.*, **42**, 1336 (1950).
- Satterfield, C. N.: "Mass Transfer in Heterogeneous Catalysis," p. 171, M. I. T. Press, Mass (1970).
- Uemura, Y., Y. Hatate and A. Ikari: *J. Japan Petrol. Inst.*, **29**, 143 (1986).
- Vincent, R. C. and R. P. Merrill: *J. Catal.*, **35**, 206 (1974).